JACS
JOURNAL OF THE AMERICAN CHEMICAL SOCIETY
Article
pubs.acs.org/JACS

Understanding Growth Kinetics of Nanorods in Microemulsion: A Combined Fluorescence Correlation Spectroscopy, Dynamic Light Scattering, and Electron Microscopy Study

Soma Sharma,[†] Nibedita Pal,[‡] Pramit K. Chowdhury,[†] Sobhan Sen,*[,‡] and Ashok K. Ganguli*[,†]

[†]Department of Chemistry, Indian Institute of Technology, Hauz Khas, New Delhi 110016, India
[‡]Spectroscopy Laboratory, School of Physical Sciences, Jawaharlal Nehru University, New Delhi 110067, India

Supporting Information

ABSTRACT: Even though nanostructures of various shapes and sizes can be controlled by microemulsions, there is substantial difficulty in understanding their growth mechanism. The evolution of nanostructures from the time of mixing of reactants to their final stage is a heterogeneous process involving a variety of intermediates. To obtain a deeper insight into these kinetic steps, we studied the slow growth kinetics (extending over eight days) of iron oxalate nanorods inside the polar core of water-in-oil microemulsion droplets made of cetyltrimethylammonium bromide/1-butanol/isooctane. Fluorescence correlation spectroscopy (FCS), dynamic light scattering (DLS), and transmission electron microscopy (TEM) have been employed to monitor the nanostructure growth at (near) the single-droplet level and in an ensemble. Analyzing FCS data with suitable kinetic model we obtain transient dimer lifetime (28 μs) and the droplet fusion rates (and fusion tendency) on each day as the reaction proceeds. The droplet fusion rate is found to directly control the nanorod growth in microemulsion solution and attains its maximum value (3.55×10^4 s^{-1}) on day 6, when long nanorods are found in TEM data, implying that more and more reactants are fed into the growing system at this stage. Combining FCS, DLS, and TEM results, we find three distinct periods in the entire growth process: a long nucleation-dominant nanoparticle growth period which forms nanoparticles of critical (average) size of ~53 nm, followed by a short period where isotropic nanoparticles switch to anisotropic growth to form nanorods, and finally elongation of nanorods and growth (and shrinking) of nanoparticles.

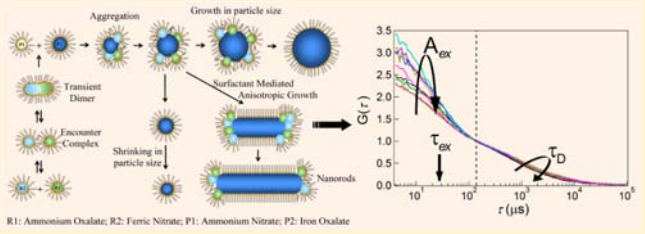

INTRODUCTION

The shapes and sizes of nanocrystals are often controlled by reaction condition, rate of nucleation, and particle aggregation.[1−5] These nanostructures have wide variety of applications in nanoscience and nanotechnology.[6−11] Following a proper synthesis route, it is possible to control the size and shape of nanocrystals.[1,12−14] However, understanding the mechanism of how reactants combine and grow into different nanostructures is still difficult.[5] This paper tackles the above problem and shows how fluorescence correlation spectroscopy (FCS) can be combined with dynamic light scattering (DLS), and transmission electron microscopy (TEM) to obtain a detailed understanding of the growth mechanism of nanostructures in a microemulsion-based synthesis.

Several growth mechanisms are proposed for different nanostructures in solution.[15−20] Takesue et al. found long nucleation-dominant growth for silver nanoparticles,[15] Edgar et al. observed that gold nanoparticles and nanorods can grow simultaneously and coexist in solution during the entire period of synthesis.[16] Earlier experiments on gold nanostructures also support this fact.[21,22] Edgar et al. proposed a "popcorn"-type stochastic growth mechanism for gold nanostructures in aqueous micellar solution.[16] However, general perception of nanorod growth mechanism is there should be a long nucleation-dominant period for nanoparticles to grow before they can switch to grow into nanorods. Our combined FCS, DLS, and TEM measurements indeed find such long nucleation-dominant growth period for iron oxalate nanoparticles, but no nanorod formation, in the initial period of synthesis. And as the nanoparticles reach their critical (average) size of ~53 nm (radius), most particles are found to switch their growth into nanorods. However, beyond this stage, some nanoparticles are seen to coexist and grow (or shrink) in size along with the growing iron oxalate nanorods. This finding suggests that the mechanism proposed by Edgar et al. may partly be applicable for colloidal nanostructures other than gold.[16]

Template methods are ideal for fabricating various nanostructures in solution.[1,7] Soft template methods, based on micelles and reverse micelles, are found to be very effective for this purpose.[1,4,7,12,13,16,23−25] In these methods, the chemical reaction occurs either at the micellar interface or inside the polar core of reverse micelles, where the surfactant molecules

Received: July 5, 2012
Published: November 12, 2012

   dx.doi.org/10.1021/ja306556e | J. Am. Chem. Soc. 2012, 134, 19677−19684

Scheme 1

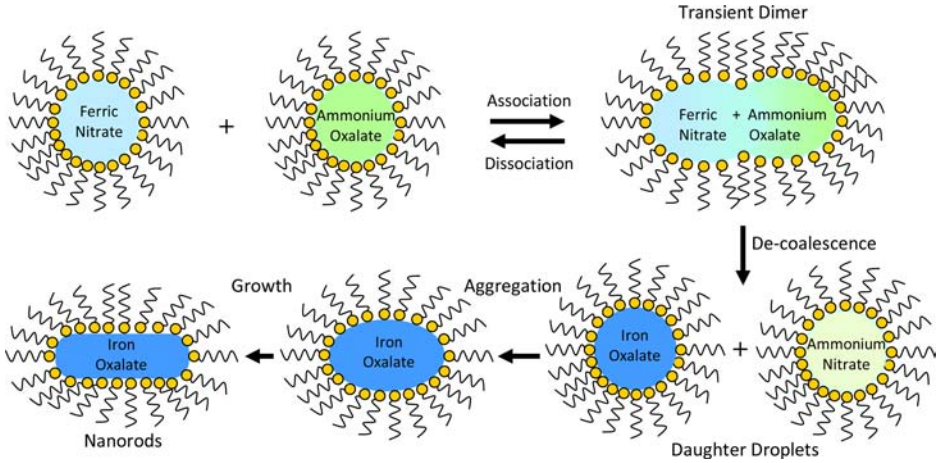

act as the templating agents for the growing nanocrystals. Cetyltrimethylammonium bromide (CTAB) is known to be an effective surfactant for this purpose because it has optimum steric properties and high affinity to bind to nanocrystal surfaces.[4,12,13,16,23−25] In aqueous solution, CTAB can also assist the growth of gold nanorods by forming a bilayer around the growing nanostructure.[26] However, in *water-in-oil* microemulsion-based reactions the surfactants form a single layer to assist the nanocrystal growth inside the polar core of microemulsion droplets (MDs) (Scheme 1).[1,4,27−37] Here, CTAB (cationic surfactant) acts as a template and plays an important role in the growth kinetics of these nanorods.

MDs are thermodynamically stable systems which consist of two immiscible liquids stabilized by a surfactant layer at their interface.[38] These droplets have the capability to encapsulate large amount of polar liquids in their core. The size of the core is controlled by a parameter, W_0 (= [polar liquid]/[surfactant]).[38] Several studies have been performed to understand the molecular interactions and dynamics in MDs.[39−44] Because of their rich phase diagrams, MDs can adopt a variety of structural architectures to assist the nanocrystal growth inside their core.[35,36] Hence, MDs are used extensively not only in nanoparticle synthesis[4,24,25,27−37] but also in purification, extraction of biomolecules,[45] and drug delivery.[46]

In solution, MDs can collide with each other and coalesce occasionally during their random motion to form a complex that is termed a "transient dimer" (Scheme 1).[4,20,47−49] The synthesis of nanostructures inside the MD starts with the mixing of two MDs containing individual reactants. Upon mixing, the coalescence of droplets results in the formation of a nanochannel between them, through which intermicellar exchange of reactants takes place, and the subsequent reaction and nucleation start at the micellar edge.[4,20,48] Finally, the dimer breaks apart and forms two daughter droplets. In one of these daughter droplets the growth of nanocrystals continues (Scheme 1),[4,20,48] [Note that there can be slight variations of the figure especially after the decoalescence steps. More detailed analysis is discussed and given in Figure 6]. Thus, in MD-based synthesis, initiation of reaction occurs only during the lifetime of the dimer. Further growth of particles/rods inside the droplet core is sustained by feeding more reactants into the system through subsequent droplet coalescence. This process continues until the final product is formed. In this reaction scheme, the important rate-determining steps are the association rate of droplets to form the transient dimer and the lifetime of the dimer, during which mixing of reactants takes place.[4,20,48] Experiments and theoretical studies have been performed to follow the kinetic steps of droplet coalescence and separation, as well as the growth of nanostructures inside MDs.[20,47,49] A bivariate population balance equation model has been proposed to explain the growth kinetics of nanoparticles inside MDs.[20] Kinetic studies have also been performed to obtain the association and dissociation rates of MDs,[47,49] which indirectly predicted the lifetime of the transient dimer (τ_{ex}) as 25 μs.[47] However, to date there are no extensive kinetic studies which provide a detailed understanding of the nanostructure growth kinetics in a microemulsion-based synthesis.

In this study, we aimed to understand the kinetic steps of nanorod growth by following the formation of iron oxalate nanorods inside the polar core of CTAB MDs over eight consecutive days. FCS is employed to monitor the reaction kinetics of droplet coalescence at the single-droplet level, the process which initiates the reaction and allows the subsequent growth of nanostructures. DLS and TEM are also used to follow the nanoparticle/nanorod growth, which complement the FCS results. By analyzing FCS data with a suitable kinetic model, we were able to obtain the dimer lifetime (τ_{ex}) and association rates of droplet coalescence for eight consecutive days. Results show that the association rate of droplets directly controls the nanorod growth inside MDs. In fact, the reader will soon discover how, by combining FCS with DLS and TEM techniques, one can obtain a comprehensive understanding of the nanostructure growth kinetics in a microemulsion-based reaction scheme.

RESULTS AND DISCUSSION

FCS Data. FCS is widely used to study molecular diffusion, chemical kinetics, and molecular interactions at the single-molecule level.[50−61] In FCS, fluorescence fluctuations from a fluorophore inside a tiny observation volume (~1 fL) are correlated. These fluctuations can arise from one or both of the changes in fluorophore concentration due to translational motion into and out of the observation volume and the changes in fluorescent properties of the molecule due to interaction with its surroundings or complex formation, or both.[50−61] Thus, information on reaction kinetics and diffusion is directly obtained by correlating the fluorescence fluctuations of the

dx.doi.org/10.1021/ja306556e | J. Am. Chem. Soc. 2012, 134, 19677−19684

reporter molecule.[60,61] Here, FCS is used to monitor the reaction and growth kinetics of iron oxalate nanostructures inside MDs by correlating the fluorescence fluctuations from a dye, sulforhodamine-B (SRhB), embedded inside the MDs. (See Supporting Information (SI) for Materials and Methods.)

Figure 1 shows the correlation curves measured in the mixture of MDs containing SRhB and reactants for eight consecutive days. The curves show a distinct two-step feature on all days. This is typical of reaction-coupled diffusive correlation curves.[58−60] The separation between reaction and diffusion is obtained only if the reaction time (τ_{ex}) becomes faster than the diffusion time (τ_D) of particles,[58,60] as in the present study. In the measured curves (Figure 1), the correlation in the faster time range (up to ∼150 μs) is fully controlled by the reaction kinetics, that is, the association and dissociation of droplets to form or break the transient dimer. The later part (beyond ∼150 μs) represents pure diffusion of the droplets (Figure 1 inset). (Note that the triplet conversion for SRhB occurs in ∼1 μs, which is much faster than the reaction time (τ_{ex}) found here.)

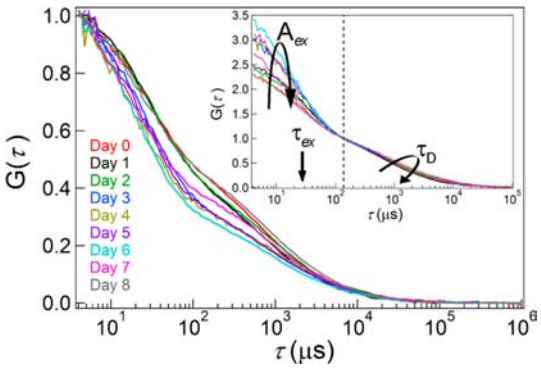

Figure 1. Raw fluorescence correlation curves measured in the reaction mixture for eight consecutive days. Curves show two distinct steps. Inset shows same raw curves when normalized at 150 μs. This plot separates the reaction and diffusion terms. The amplitude (A_{ex}) of the reaction term increases until day 6 and then decreases. The diffusion term shows a similar feature. Arrows indicate the direction of change of the two processes.

Droplet Interaction Kinetics. On day 0, mixing of equimolar microemulsions containing reactants and SRhB, the droplets start colliding with each other and form an intermediate encounter complex that coalesces to form the transient dimer (Scheme 2).[4,20,47−49] The intermicellar exchange of reactants can take place in this transient dimer. Along with the reactants, SRhB can also be exchanged between the droplets, which leads to changes in the local environment of SRhB, which in turn modulate its fluorescence yield from high-to-low or low-to-high. These fluctuations then get correlated and appear as a characteristic reaction term in the diffusion-coupled correlation curves. We find that the fluorescence intensity of SRhB is higher inside the droplet containing only ammonium oxalate (high-state, ↑) than inside the droplet containing only ferric nitrate (low-state, ↓). The lower fluorescence yield of SRhB in the presence of ferric nitrate may arise from iron-induced fluorescence quenching. The inset of Figure 1 distinctly shows the two regions of reaction and diffusion, when the curves are normalized at 150 μs. This plot clearly shows that the amplitude (A_{ex}) of the reaction term increases with time until day 6, and then decreases. This suggests that there must be a strong interrelation between droplet coalescence and nanostructure formation inside the droplets. In fact, we do find such an interrelation (see below). It should be noted that the two-step feature in correlation plots is not seen in the measured curves for MDs containing only pre-dissolved reactants (see Figures S3 and S4).

Scheme 2

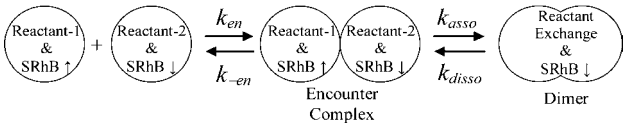

The droplet interaction kinetics can be visualized as a two-step reaction as in Scheme 2.[20,47,49] Here, k_{en} and k_{-en} are the forward and backward rates for the formation and separation of the encounter complex. These rates are generally very high, and are diffusion controlled within the Smoluchowski limit.[47] Among many encounter complexes, few (1 in ∼5000) can coalesce to form the transient dimer where exchange of reactants can take place.[47] In the second step of the reaction, k_{asso} and k_{disso} are defined as the association and dissociation rates of the droplets, respectively, which control the rate of formation and breaking of the transient dimer. Thus, in FCS, we only see the second step of the reaction where the transient dimer is formed, but not the first one where encounter complex is formed. Moreover, the first step occurs in tens of nanoseconds,[47] which falls beyond the dynamic range of the current FCS setup.

On day 0, the reaction is initiated by adding equal amounts of microemulsions, containing equimolar reactants. No extra reactant is added later. Thus, the observed change in the reaction kinetics can be explained by the time-dependent change in the association and dissociation rates of droplets that form or break the dimer. This second stage of the reaction can be treated as a simple first-order reaction where the encounter complex proceeds to form the dimer and vice versa. Under this condition, the equilibrium constant (K) and the reaction time (τ_{ex}) for droplet fusion and breaking can be written in terms of k_{asso} and k_{disso} as[47,59]

$$K = \frac{k_{asso}}{k_{disso}} \quad \text{and} \quad \tau_{ex} = (k_{asso} + k_{disso})^{-1} \tag{1}$$

The reaction-coupled diffusive correlation curves then can be modeled as[58−60]

$$G(\tau) = \frac{1}{N}\left(1 + \frac{\tau}{\tau_D}\right)^{-1}\left(1 + \left(\frac{r}{l}\right)^2\left(\frac{\tau}{\tau_D}\right)\right)^{-1/2} \times (1 + A_{ex}\, e^{-\tau/\tau_{ex}}) \tag{2}$$

where N is the average number of particles in the observation volume, τ_{ex} is the characteristic reaction time of droplet fusion (lifetime of transient dimer), and A_{ex} is the amplitude of the reaction. If the ratio of quantum yields of the low state and high state of SRhB is given by $Q = Q_{low}/Q_{high}$, the amplitude (A_{ex}) can then be written as[59]

$$A_{ex} = K\left(\frac{1 - Q}{1 + KQ}\right)^2 \tag{3}$$

dx.doi.org/10.1021/ja306556e | J. Am. Chem. Soc. 2012, 134, 19677−19684

Reaction and Growth of Nanostructures inside MDs. Equation 2, substituted with eqs 1 and 3, is used to model FCS data for most systems in order to extract the reaction time and the size information through diffusion parameters. However, earlier FCS and DLS studies found broad size distributions for MDs in solution.[61,62] Pal et al. found that FCS data of MDs can be analyzed by assuming a Gaussian distribution of diffusion times.[61] However, we found that the present correlation data could be fitted satisfactorily by assuming a *bimodal* Gaussian distribution in particle diffusions (Figure 2A). This is consistent

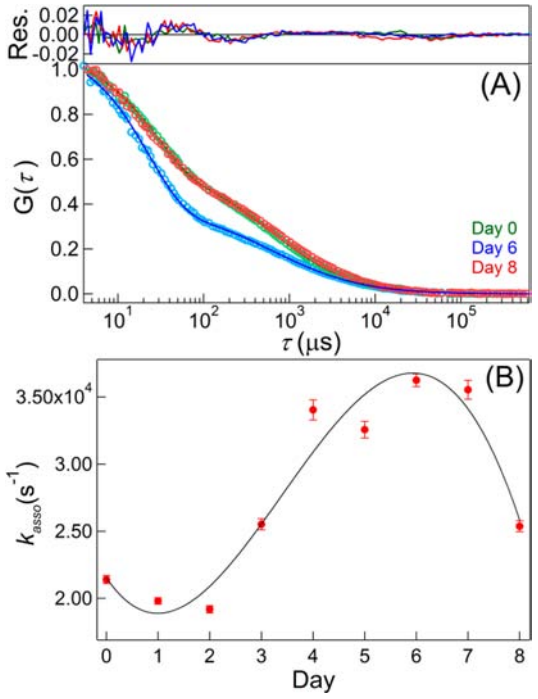

Figure 2. (A) Fluorescence correlation curves fitted with eq 4, incorporating expressions of τ_{ex} and A_{ex}. Residuals of fits are plotted in the top panel. Only three curves are shown here for clarity. The fits to other data give similar residuals. Fits extracted $Q \approx 0.09$ on all eight days. (B) Variation of association rate (k_{asso}) of droplets with time. Initially, k_{asso} decreases (slightly) until day 2, but then increases significantly and reaches a maximum on day 6 (see text). For the time-dependent change in K, see SI.

with the physical characteristics of the present microemulsion system: During the reaction, products formed inside daughter droplets that are larger in size than the droplets containing only reactants. Thus, the data were fit to eq 4, incorporating expressions from eq 1 and 3 and a *bimodal* distribution of $a_i(\tau_{Di})$:

$$G(\tau) = \sum_{i=1}^{m} a_i \left(1 + \frac{\tau}{\tau_{Di}}\right)^{-1} \left(1 + \left(\frac{r}{l}\right)^2 \left(\frac{\tau}{\tau_{Di}}\right)\right)^{-1/2} \times \left(1 + A_{ex}\, e^{-\tau/\tau_{ex}}\right) \quad (4)$$

where

$$a_i(\tau_{Di}) = B_{1i} \exp\left(-\left(\frac{\ln(\tau_{Di}) - \ln(\tau_{1p})}{b_1}\right)^2\right) + B_{2i} \exp\left(-\left(\frac{\ln(\tau_{Di}) - \ln(\tau_{2p})}{b_2}\right)^2\right)$$

In eq 4, B_{1i} and B_{2i} are the relative contributions of components of the two distributions, τ_{1p} and τ_{2p} are the peak diffusion times, and b_1 and b_2 are related to the widths of distributions.[61] Least-squares fitting is performed using eq 4 with τ_{ex} and A_{ex} expressions from eqs 1 and 3, in which K, k_{asso}, and Q, as well as B_i's and b_i's, were varied to get the best distribution of $a_i(\tau_{Di})$.[61] Figure 2A shows the data fitted with eq 4.

The importance of the present study lies in the fact that FCS unravels the entire reaction kinetics by following the droplet coalescence and de-coalescence process at or near the single-droplet level. The dimer lifetime (τ_{ex}) extracted from fitting the FCS data using eq 4 is found to be ~28 μs, which is almost constant during eight days. Earlier, Robinson and co-workers indirectly predicted the dimer lifetime to be ~25 μs for Aerosol-OT (AOT) MDs on the basis of electron- and proton-transfer reactions and metal−ligand interactions in the ensemble of MDs.[47] Here we show that FCS can directly provide this dimer lifetime (τ_{ex}). In a recent report, Orden, Levinger, and co-workers reported the droplet interaction times using FCS by monitoring the fluorescence fluctuations of Cyanine-3 inside AOT MDs.[49] They found two reaction time constants, one of which extracts a value <20 μs and the other ~1 μs.[49] However, it is difficult to explain the origin of the two time constants, because the variation in correlation data is observable only within ~2 μs. Our FCS data, however, show correlation up to ~150 μs, which arises from reaction, and give the reaction time as ~28 μs, which is similar to the value predicted by Robinson and co-workers.[47] However, it should be noted that the sizes of reactant-containing reverse micelles in our study (~9 nm) are larger than those used by Orden, Levinger, and co-workers (~2−4 nm),[49] which might lead to the observed changes in the droplet interaction times.

Incorporating the expressions from eqs 1 and 3 into eq 4, the time-dependent association rates (and equilibrium constant, K) of droplet interactions were determined directly from FCS. Results show that the association rate (k_{asso}) of droplet coalescence first decreases by a small amount until day 2, and then increases significantly until day 6, when it reaches the maximum value, $k_{asso} = 3.55 \times 10^4$ s^{-1} (Figure 2B). However beyond day 6, this rate continues to decrease. Similarly, the equilibrium constant (K), which defines the tendency of droplet fusion, also increases with time until day 6 and then decreases (Figure S5). This finding is fascinating owing to the fact that in TEM studies we see long nanorods starting to form on day 6 (see below). This implies that the maximum number of reactant-containing droplets are interacting with the growing nanorod, which increases the aspect ratio of these nanorods, as confirmed by TEM studies. The gradual increase in k_{asso} (and K) in initial days also suggests the existence of long nucleation-dominant nanoparticle growth through droplet coalescence, which leads to isotropic nanoparticles until a critical size of ~53 nm, beyond which they grow anisotropically to form nanorods. The overall process clearly depicts how the MDs kinetically control the formation of nanostructures by modulating the

dx.doi.org/10.1021/ja306556e | J. Am. Chem. Soc. 2012, 134, 19677−19684

droplet interactions and feeding different amounts of reactants into the reaction system at different stages of the growth.

The existence of nucleation-dominant nanoparticle growth is confirmed by the shift in particle size distributions toward larger size with time. The results show two distinct distributions of diffusion times beyond ~150 μs: one on a lower time scale, indicating free diffusion of droplets containing only pre-dissolved reactants or byproduct (ammonium nitrate), or both, and the other following the growth kinetics of iron oxalate nanoparticles inside the droplets. The distributions of hydrodynamic radii (R_h) of droplets were calculated from the distributions of diffusion times using the Stokes–Einstein equation (SI). The actual sizes of nanoparticles (and by-product/reactants) are then calculated by subtracting the thickness of the CTAB surfactant layer (~2 nm)[63] from the R_h distributions of the droplets, as plotted in Figure 3A. A

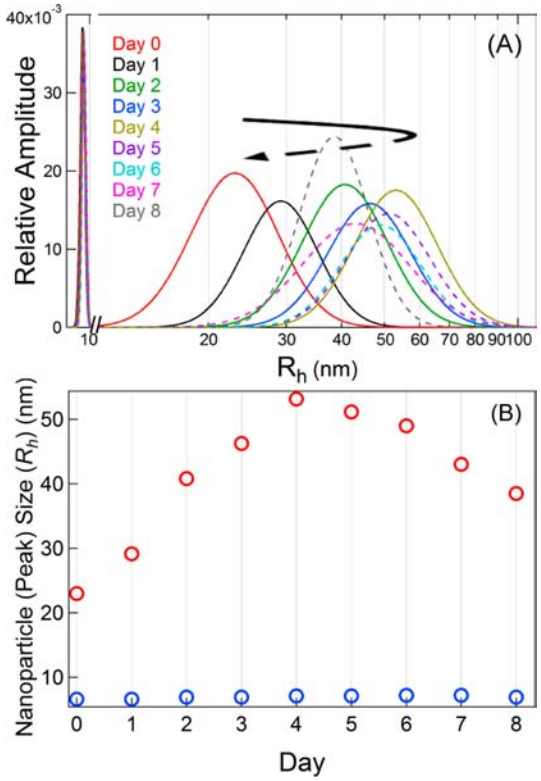

Figure 3. (A) Size distributions of nanoparticles obtained on each day from the FCS data. Distributions near ~7 nm denote the sizes of MDs containing only reactants/byproducts. Distributions in the larger size range show the change in particle size with time. Arrow indicates the direction of size variation with time. (B) Change in peak sizes of the two distributions with time. Plot shows that nanoparticles reach their critical size of ~53 nm on day 4. The sizes of smaller particles stay almost constant (~7 nm) with time. See Table 1 for the values.

closer look reveals that smaller droplets (peak radii of ~9 nm) do not change their size with time. This indicates that the size of droplets containing only pre-dissolved reactants and/or byproduct remains constant over the entire synthesis period (droplets containing independent reactants are found to be ~9–12 nm). However, the other distribution shows a monotonic shift in its peak position toward higher values along with an increase in full width at half-maximum (FWHM) with time, indicating the growth of nanocrystals inside droplets. This shift toward larger size is observed until day 4, beyond which it decreases. The day-to-day variation of droplet sizes (Figure 3B) distinctly shows that nanoparticles grow up to an average size of ~53 nm on day 4, and then only smaller particles are observed. These smaller nanoparticles can arise from the redistribution/reprecipitation of fragmented rods/particles. In fact, it is found that beyond the critical size (~53 nm), most particles switch to anisotropic nanorods. This phenomenon is supported by the TEM data, as we start seeing the formation of small nanorods on day 5 (see below). It should be noted here that FCS could not detect the MDs containing large nanorods/nanoparticles because they mostly settle at the bottom, and even if they diffuse slowly through solution, no detectable fluorescence fluctuations are observed from these nanostructures as their sizes become comparable to the size of the focused laser spot.

DLS Data. Although FCS unfolds the trend of nanostructure growth, to further confirm these results DLS is employed to characterize the system at the ensemble level. The peak hydrodynamic radius (R_h) of droplets containing ferric nitrate is found to remain almost constant on all days (~8 nm), similar to that obtained in FCS (~9 nm). DLS data for droplets containing ammonium oxalate give $R_h \approx 12.5$ nm, also similar to that obtained from FCS data. DLS studies were carried out to look at the *in situ* growth kinetics of iron oxalate nanostructures in microemulsion solution. We found DLS can detect large nanostructures (possibly the nanorods) on and after day 5. To confirm the above, we analyzed the DLS data incorporating the asymmetry of anisotropic nanorods in the expression of diffusion constant (see SI).[64,65] Using the diameter of the nanorods obtained from TEM data, we calculate the distributions in nanorod lengths (see Figure S2 and Table 1 below). Although the calculated distribution for length does not match perfectly with the lengths obtained through TEM studies, the data do confirm that DLS can detect large nanostructures in the later stages (beyond day 4) of the synthesis. In an ensemble it is possible that many MDs containing rods (and particles) associate to form large aggregates which are mainly detected in the *in situ* DLS measurements, rather than the single nanorods. Moreover, the rods may have a distribution in size (diameter) which is difficult to ascertain in DLS. Even though *in situ* DLS measurements could detect large nanostructures, it could not detect the nucleation-dominant nanoparticle growth in the initial days (until day 4), but was only detecting the smaller particles (see Figure S6A). This could be due to the availability of fewer MDs containing the nucleated particles which have very low (total) scattered intensity to be detected in DLS. However, these growing nanoparticles were easily detected in FCS and TEM measurements. Interestingly, however, when DLS measurements were performed on iron oxalate nanoparticles extracted from the reaction mixture and redispersed in ethanol, we observed an increasing trend of nanoparticle growth matching with the FCS and TEM results (see Figure S6B, Figure 5, and Table 1 below). The growth of nanoparticles is found to continue beyond day 5. This indicates that DLS could detect the larger nanoparticles beyond day 5 if they were extracted from the mixture and redispersed in ethanol. It is also found that the heterogeneity in particle size (FWHM) is maximum on day 6 (Figure S6B), which indicates that on this day a large number of droplets associate to shift the equilibrium from particles to rods.

It is important to note here that the simultaneous growth (or shrinking) of nanorods and nanoparticles beyond day 5

dx.doi.org/10.1021/ja306556e | J. Am. Chem. Soc. 2012, 134, 19677–19684

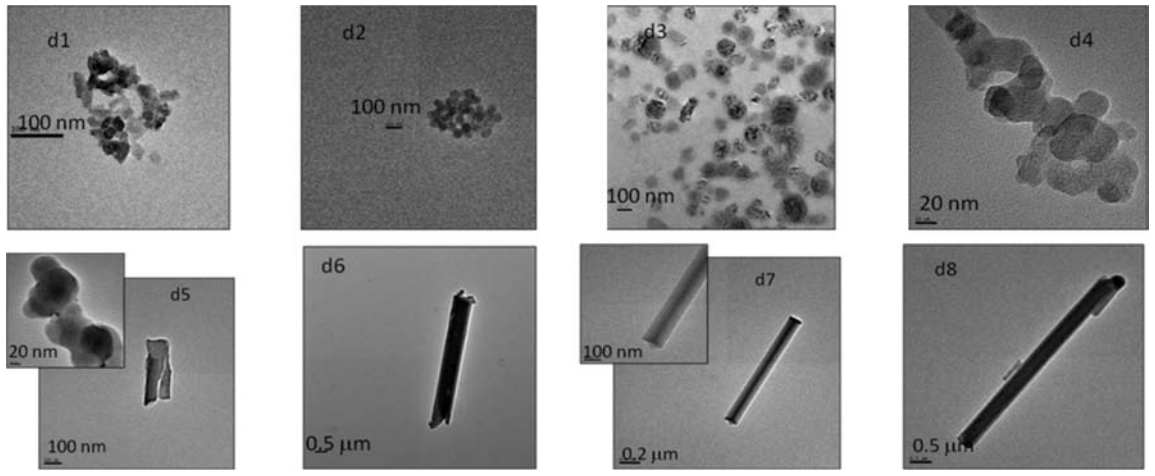

Figure 4. TEM images for the growing nanocrystals as obtained on eight consecutive days. Until day 4 the nanoparticles grow monotonically. On day 4 the particles are seen to start aggregating to form the small nanorods on day 5. On day 6 onward the nanorods grow in length very fast. Fully grown nanorods are seen on day 8.

Table 1. Size Parameters of Nanostructures Obtained from FCS, DLS, and TEM Measurements

	FCS[a]				DLS						TEM			
	first distribution		second distribution		*in situ*[a]				nanoparticles redispersed in ethanol		nanoparticles	nanorods		
day	peak size (nm)	FWHM (nm)	peak size (nm)	FWHM (nm)	peak size (nm)	FWHM (nm)	peak[b] rod length (nm)	FWHM of length (nm)	peak size (nm)	FWHM (nm)	size (nm)	length (nm)	diam (nm)	aspect ratio
0	7	2	23	12	7	2.5	–	–	–	–	–	–	–	–
1	7	2	29	12	7	3	–	–	35	7	28 (±4)	–	–	–
2	7	2	41	21	7	3	–	–	46	8	42 (±10)	–	–	–
3	7	2	46	23	7	3	–	–	48	12	50 (±6)	–	–	–
4	7	2	53	27	6	3	–	–	53	9	57 (±5)	–	–	–
5	7	2	51	26	–	–	15000	6000	61	11	70 (±15)	350	115	3:1
6	7	2	49	25	–	–	15000	8000	73	24	60 (±15)	3900	540	7:1
7	7	2	44	29	–	–	9000	4000	85	21	–	5000	490	10:1
8	7	2	39	17	–	–	22000	6000	94	20	–	5400	390	14:1

[a]Particle sizes are calculated by subtracting the thickness (2 nm) of CTAB surfactant layer from the size distribution of MDs. [b]Values calculated by considering the asymmetry of nanorods and taking diameters of nanorods from column 14 (see SI).

supports the prediction of Edgar et al., which suggests that particles and rods can grow simultaneously in solution if few isotropic nanoparticles break their symmetry to grow anisotropically to form nanorods,[16] but the rest of the particles which do not undergo the symmetry breaking can grow normally.[16] In the case of gold it is proposed that if particles of less than ∼5 nm break their symmetry, they can grow into nanorods.[16] A similar argument might be applicable for the present iron oxalate nanostructures, as they also show similar bifurcation near the critical particle size of ∼53 nm. However, contrary to the prediction of Edgar et al., nanorods were not detected in any of the measurements in the initial days of the 8-day reaction. This suggests that the iron oxalate nanorods can grow only when the nucleated nanoparticles reach their critical size of ∼53 nm.

TEM Data. To investigate the growth kinetics and formation of nanorods starting from nucleated nanoparticles, we carried out TEM measurements on iron oxalate nanostructures formed in the reaction mixture on each day. Figure 4 shows the recorded evolution of nanostructures with time. In these images we see the growth of uniform nanoparticles in the initial days. During the nucleation-dominant period the nanoparticles increase their size relatively faster, and on day 5 they start growing into nanorods. Interestingly, on day 5 the TEM image shows a mixture of nanorods and nanoparticles, indicating the co-existence of nanoparticles and nanorods. Particles were also detected on day 6 (see Table 1), though the equilibrium shifts more toward the formation of nanorods. In FCS we observe the highest association rate of droplets on day 6, which suggests at this stage the nanoparticles rapidly switch their symmetry to form the anisotropic nanorods, as is seen in the TEM images. The aspect ratio of the nanorod increases with time from 3:1 (day 5) to 14:1 (day 8). This implies that there is a more attractive interaction between the particles along the longer axis compared to the lateral axis of the rods that leads to the increase in aspect ratio. Such an increase originates from the fact that CTAB decreases the surface charge density of the ionic micelles and thereby promotes the formation of low-curvature micellar geometries like nanorods.[66] Thus, it is suggested that, due to positive surface charges, these cationic surfactants assemble on the surface of the growing nanostructure[33] (due to negative zeta potential) and subsequently allow the growth along the long axis, leading to the formation of long nanorods.

dx.doi.org/10.1021/ja306556e | J. Am. Chem. Soc. 2012, 134, 19677−19684

Table 1 compares the size parameters obtained from FCS, DLS, and TEM measurements. These data show that, during the nucleation-dominant nanoparticle growth, FCS, DLS, and TEM find similar particle sizes. However, when the particles reach their critical size of ∼53 nm, most of them aggregate to form nanorods, and the rest of the particles grow in size or shrink to smaller ones. These size parameters are plotted together in Figure 5 for a comprehensive understanding of the growth mechanism.

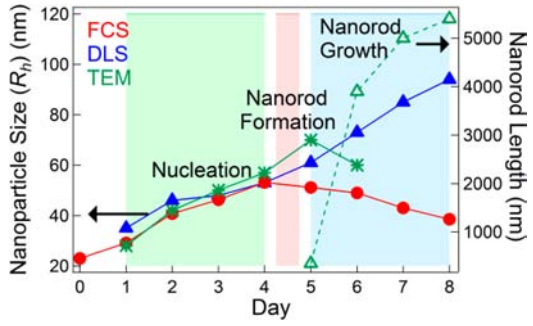

Figure 5. Combined plot of time-dependent size parameters of nanocrystals obtained from FCS, DLS, and TEM. Three distinct periods are noticed for the entire nanostructure growth. Red curve shows sizes obtained from FCS, blue curve denotes DLS data obtained for re-dispersed nanoparticles in ethanol, and green curves show TEM data; the green dotted-line curve with open triangles denotes the change in nanorod lengths seen in TEM images.

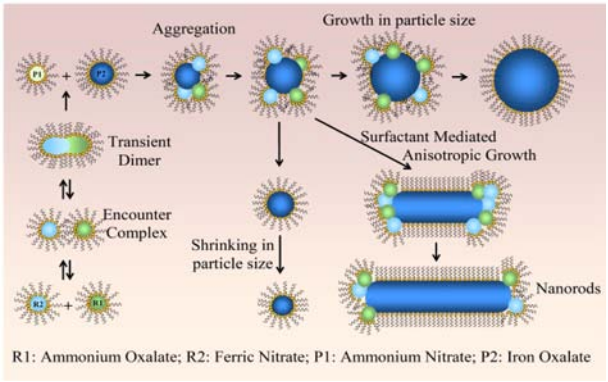

Figure 6. Growth mechanism of iron oxalate nanoparticles and nanorods inside the polar core of MDs. Droplets containing reactants interact to first produce an intermediate encounter complex. This encounter complex fuses to form the transient dimer, which then produces the daughter droplets. Inside one of these daughter droplets, the growth of nanocrystals continues.

The plot clearly shows three distinct periods through which iron oxalate nanorods are formed: a long nucleation-dominant nanoparticle growth period in initial days, then a short period where nanoparticles start forming nanorods, and finally growth (and shrinking) of nanoparticles simultaneous with the growth of nanorods. Figure 6 depicts a possible mechanism of how MDs interact to coalesce and exchange reactants with time to grow the nanostructures. From the start of the reaction until day 4, FCS, DLS, and TEM measured similar sizes of the growing nanoparticles, signifying the existence of long nucleation-dominant particle growth (Figure 5). During days 4 and 5, the particles undergo symmetry breaking and start forming nanorods. On and after day 5, FCS starts finding the smaller particles, and TEM starts showing the formation of nanorods. DLS can, however, find bigger particles with passing time if they are separated and redispersed in ethanol (Figure 5). In TEM, the growth in nanorod length and aspect ratio changes drastically from day 5 to day 6 (Figure 4 and Table 1). This observation is supported by FCS results which show that, on day 6, the rate of droplet coalescence reaches its maximum to feed the highest reactants into the growing nanorod system.

CONCLUSIONS

A detailed and comprehensive study has been carried out on the growth kinetics of iron oxalate nanorods as they formed over several days inside the water pool of CTAB MDs in isooctane. To date, there are no extensive experimental studies on nanostructure formation in microemulsion-based reactions that can explain the crucial role of droplet interactions in the reaction kinetics. FCS, DLS, and TEM measurements have been carried out over several days to follow the entire growth kinetics of iron oxalate nanorods starting from their particle nucleation. Analyzing the FCS data with a suitable kinetic model, the droplet coalescence time or dimer lifetime (∼28 μs) was extracted along with the droplet association rate and the equilibrium constant of the chemical reaction. The droplet association rate showed an interesting time-dependent feature that directly connects it to the growth mechanism. Combining FCS, DLS, and TEM, we found three distinct periods in the entire nanorod growth kinetics: a long nucleation-dominant nanoparticle growth period, followed by a short period where isotropic nanoparticles switch over to anisotropic growth to form nanorods, and finally the period where droplet-association-assisted elongation of nanorods is observed. We have shown here how one can utilize the single-molecular FCS technique, together with DLS and TEM, to obtain a comprehensive insight on the growth mechanism of nanorods in a microemulsion-based reaction scheme. The detailed methodologies discussed in this study are unique in their kind, and can be used to understand the growth kinetics of other desired nanostructures which are required for various applications in nanoscience and nanotechnology.

ASSOCIATED CONTENT

Supporting Information

Materials and methods, supporting data, and text. This material is available free of charge via the Internet at http://pubs.acs.org.

AUTHOR INFORMATION

Corresponding Author

ashok@chemistry.iitd.ac.in; sens@mail.jnu.ac.in

Notes

The authors declare no competing financial interest.

ACKNOWLEDGMENTS

This work is supported by DST (Nano Mission. SR/NM/NF95/2010), DeitY (12(4)/2007-PDD), and DST (SR/FTP/PS-16/2007), Govt. of India. S. Sen thank Prof. S. Maiti for helpful technical discussions on FCS setup as well as for providing the data collection software. S. Sharma and N. Pal thank CSIR for providing fellowships.

REFERENCES

(1) Burda, C.; Chen, X.; Narayanan, R.; El-Sayed, M. A. *Chem. Rev.* **2005**, *105*, 1025−1102.

(2) Manna, L.; Scher, E. C.; Alivisatos, A. P. *J. Am. Chem. Soc.* **2000**, *122*, 12700−12706.
(3) Peng, X.; Manna, L.; Yang, W.; Wickham, J.; Scher, E.; Kadavanich, A.; Alivisatos, A. P. *Nature* **2000**, *404*, 59−61.
(4) Ganguli, A. K.; Ganguly, A.; Vaidya, S. *Chem. Soc. Rev.* **2010**, *39*, 474−485.
(5) Kumar, S.; Nann, T. *Small* **2006**, *2*, 316−329.
(6) Kroutvar, M.; Ducommun, Y.; Heiss, D.; Bichler, M.; Schuh, D.; Abstreiter, G.; Finley, J. J. *Nature* **2004**, *432*, 81−84.
(7) Murphy, C. J.; Gole, A. M.; Stone, J. W.; Sisco, P. N.; Alkilany, A. M.; Goldsmith, E. C.; Baxter, S. C. *Acc. Chem. Res.* **2008**, *41*, 1721−1730.
(8) Huang, J.; Jackson, K. S.; Murphy, C. J. *Nano Lett.* **2012**, *12*, 2982−2987.
(9) Liu, B.; Aydil, E. S. *J. Am. Chem. Soc.* **2009**, *131*, 3985−3990.
(10) Kern, S. J.; Sahu, K.; Berg, M. A. *Nano Lett.* **2011**, *11*, 3493−3498.
(11) Huynh, W. U.; Dittmer, J. J.; Alivisatos, A. P. *Science* **2002**, *295*, 2425−2427.
(12) Sau, T. K.; Murphy, C. J. *J. Am. Chem. Soc.* **2004**, *126*, 8648−8649.
(13) Gou, L.; Murphy, C. J. *Chem. Mater.* **2005**, *17*, 3668−3672.
(14) Hao, E.; Bailey, R. C.; Schatz, G. C.; Hupp, J. T.; Li, S. *Nano Lett.* **2004**, *4*, 327−330.
(15) Takesue, M.; Tomura, T.; Yamada, M.; Hata, K.; Kuwamoto, S.; Yonezawa, T. *J. Am. Chem. Soc.* **2011**, *133*, 14164−14167.
(16) Edgar, J. A.; McDonagh, A. M.; Cortie, M. B. *ACS Nano* **2012**, *6*, 1116−1125.
(17) Lemyre, J.-L.; Lamarre, S.; Beaupre, A.; Ritcey, A. M. *Langmuir* **2011**, *27*, 11824−11834.
(18) Peng, X. *Adv. Mater.* **2003**, *15*, 459−463.
(19) Xu, X.; Liu, F.; Yu, K.; Huang, W.; Peng, B.; Wei, W. *ChemPhysChem* **2007**, *8*, 703−711.
(20) Ethayaraja, M.; Bandyopadhyaya, R. *J. Am. Chem. Soc.* **2006**, *128*, 17102−17113.
(21) Sau, T. K.; Murphy, C. J. *Langmuir* **2004**, *20*, 6414−6420.
(22) Niidome, Y.; Nishioka, K.; Kawasaki, H.; Yamada, S. *Chem. Commun.* **2003**, *18*, 2376−2377.
(23) Pérez-Juste, J.; Liz-Marzán, L. M.; Carnie, S.; Chan, D. Y. C.; Mulvaney, P. *Adv. Funct. Mater.* **2004**, *14*, 571−579.
(24) Vaucher, S.; Li, M.; Mann, S. *Angew. Chem., Int. Ed.* **2000**, *39*, 1793−1796.
(25) Ganguli, A. K.; Ahmad, T. *J. Nanosci. Nanotechnol.* **2007**, *7*, 2029−2035.
(26) Nikoobakht, B.; El-Sayed, M. A. *Langmuir* **2001**, *17*, 6368−6374.
(27) Boutonnet, M.; Kizling, J.; Stenius, P.; Maire, G. *Colloids Surf.* **1982**, *5*, 209−225.
(28) Naoe, K.; Petit, C.; Pileni, M. P. *Langmuir* **2008**, *24*, 2792−2798.
(29) Boutonnet, M.; Lögdberg, S.; Svensson, E. E. *Curr. Opin. Colloid Interface Sci.* **2008**, *13*, 270−286.
(30) Joselevich, E.; Willner, I. *J. Phys. Chem.* **1994**, *98*, 7628−7635.
(31) Zarur, A. J.; Ying, J. Y. *Nature* **2000**, *403*, 65−67.
(32) Petit, C.; Lixon, P.; Pileni, M. P. *J. Phys. Chem.* **1990**, *94*, 1598−1603.
(33) Ganguli, A. K.; Ahmad, T.; Vaidya, S.; Ahmed, J. *Pure Appl. Chem.* **2008**, *80*, 2451−2477.
(34) Ahmed, J.; Kumar, B.; Mugweru, A. M.; Trinh, P.; Ramanujachary, K. V.; Lofland, S. E.; Govind; Ganguli, A. K. *J. Phys. Chem. C* **2010**, *114*, 18779−18784.
(35) Eastoe, J.; Hollamby, M. J.; Hudson, L. *Adv. Colloid Interface Sci.* **2006**, *128*−*130*, 5−15.
(36) Ranjan, R.; Vaidya, S.; Thaplyal, P.; Qamar, M.; Ahmed, J.; Ganguli, A. K. *Langmuir* **2009**, *25*, 6469−6475.
(37) Vaidya, S.; Rastogi, P.; Agarwal, S.; Gupta, S. K.; Ahmad, T.; Antonelli, A. M., Jr.; Ramanujachary, K. V.; Lofland, S. E.; Ganguli, A. K. *J. Phys. Chem. C* **2008**, *112*, 12610−12615.
(38) Luisi, P. L., Straube, B. E, Eds. *Reverse Micelles*; Plenum Press: New York, 1984.
(39) Bhattacharyya, K. *Acc. Chem. Res.* **2003**, *36*, 95−101.
(40) Fayer, M. D.; Levinger, N. E. *Annu. Rev. Anal. Chem.* **2010**, *3*, 89−107.
(41) Mondal, S. K.; Ghosh, S.; Sahu, K.; Mandal, U.; Bhattacharyya, K. *J. Chem. Phys.* **2006**, *125*, 224710.
(42) Baruah, B.; Roden, J. M.; Sedgwick, M.; Correa, N. M.; Crans, D. C.; Levinger, N. E. *J. Am. Chem. Soc.* **2006**, *128*, 12758−12765.
(43) Pieniazek, P. A.; Lin, Y.-S.; Chowdhary, J.; Ladanyi, B. M.; Skinner, J. L. *J. Phys. Chem. B* **2009**, *113*, 15017−15028.
(44) Chowdhary, J.; Ladanyi, B. M. *J. Phys. Chem. B* **2009**, *113*, 15029−15039.
(45) Mazzola, P. G.; Lopes, A. M.; Hasmann, F. A.; Jozala, A. F.; Penna, T. C. V.; Magalhaes, P. O.; Rangel-Yagui, C. O.; Pessoa, A., Jr. *J. Chem. Technol. Biotechnol.* **2008**, *83*, 143−157.
(46) Trivedi, R.; Kompella, U. B. *Nanomedicine* **2010**, *5*, 485−505.
(47) Fletcher, P. D. I.; Howe, A. M.; Robinson, B. H. *J. Chem. Soc., Faraday Trans. 1* **1987**, *83*, 985−1006.
(48) López-Quintela, M. A.; Tojo, C.; Blanco, M. C.; Rio, L. G.; Leis, J. R. *Curr. Opin. Colloid Interface Sci.* **2004**, *9*, 264−278.
(49) McPhee, J. T.; Scott, E.; Levinger, N. E.; Orden, A. V. *J. Phys. Chem. B* **2011**, *115*, 9585−9592.
(50) Magde, D.; Elson, E.; Webb, W. W. *Phys. Rev. Lett.* **1972**, *29*, 705−708.
(51) Rigler, R.; Mets, Ü.; Widengren, J.; Kask, P. *Eur. Biophys. J.* **1993**, *22*, 169−175.
(52) Maiti, S.; Haupts, U.; Webb, W. W. *Proc. Natl. Acad. Sci. U.S.A.* **1997**, *94*, 11753−11757.
(53) Haustein, E.; Schwille, P. *Annu. Rev. Biophys. Biomol. Struct.* **2007**, *36*, 151−169.
(54) Shi, X.; Foo, Y. H.; Sudhaharan, T.; Chong, S.-W.; Korzh, V.; Ahmed, S.; Wohland, T. *Biophys. J.* **2009**, *97*, 678−686.
(55) Digman, M. A.; Gratton, E. *Annu. Rev. Phys. Chem.* **2011**, *62*, 645−668.
(56) Ishii, K.; Tahara, T. *J. Phys. Chem. B* **2010**, *114*, 12383−12391.
(57) Sasmal, D. K.; Mondal, T.; Mojumdar, S. S.; Choudhury, A.; Banerjee, R.; Bhattacharyya, K. *J. Phys. Chem. B* **2011**, *115*, 13075−13083.
(58) Al-Soufi, W.; Reija, B.; Novo, M.; Felekyan, S.; Kühnemuth, R.; Seidel, C. A. M. *J. Am. Chem. Soc.* **2005**, *127*, 8775−8784.
(59) Orden, A. V.; Jung, J. *Biopolymers* **2007**, *89*, 1−16.
(60) Verma, S. D.; Pal, N.; Singh, M. K.; Shweta, H.; Khan, M. F.; Sen, S. *Anal. Chem.* **2012**, *84*, 7218−7226.
(61) Pal, N.; Verma, S. D.; Singh, M. K.; Sen, S. *Anal. Chem.* **2011**, *83*, 7736−7744.
(62) Sen, S.; Dutta, P.; Sukul, D.; Bhattacharyya, K. *J. Phys. Chem. A* **2006**, *106*, 6017−6023.
(63) Palazzo, G.; Lopez, F.; Giustini, M.; Colafemmina, G.; Ceglie, A. *J. Phys. Chem. B* **2003**, *107*, 1924−1931.
(64) Tsay, J. M.; Doose, S.; Weiss, S. *J. Am. Chem. Soc.* **2006**, *128*, 1639−1647.
(65) Vasanthi, R.; Ravichandran, S.; Bagchi, B. *J. Chem. Phys.* **2001**, *114*, 7989−7992.
(66) Tornblom, M.; Henrikesson, U. *J. Phys. Chem. B* **1997**, *101*, 6028−6035.